Long-Term Atmospheric Emissions for the Coal Oil Point Natural Marine Hydrocarbon Seep Field, Offshore California

[1]Ira Leifer, [1]Chris Melton, [2]Donald Blake
[1]Bubbleology Research International
[2]University of California, Irvine

Supplemental Material

S1 The Gaussian Plume model theoretical basis

Sea surface emissions for focused bubble plumes can be described as a point source whose atmospheric plume can be modeled as a Gaussian plume (Hanna et al., 1982). The Gaussian plume model relates atmospheric emissions, E_A, to the concentration anomaly, *C*', relative to ambient, *C*, wind speed, *u*, and the atmospheric turbulence parameters, σ_y and σ_z, defined in a cartesian coordinate system where *x* is the downwind, i.e., wind direction, *θ*, *y* is the transverse direction, and *z* is the vertical coordinate,

$$C'(x,y,z) = E_A \frac{exp\left(\frac{-y^2}{2\sigma_y^2}\right)}{(2\pi u \sigma_z \sigma_y)}\left(exp\left(\frac{-(z-h)^2}{2\sigma_z^2}\right) + exp\left(\frac{-(z+h)^2}{2\sigma_z^2}\right) + exp\left(\frac{-(z-2(BL-h))^2}{2\sigma_z^2}\right) + exp\left(\frac{-(z+2(BL-h))^2}{2\sigma_z^2}\right)\right), \quad \textbf{(S1)}$$

where *h* is the measurement height. The second exponential term represents reflection off the sea surface and assumes a non-sticky molecule, the third term represents reflection off the marine boundary layer, at height *BL*, and the fourth term represents re-reflection off the surface (**Fig. S1**). A shallower boundary layer height, *BL*, contributes more significantly to this reflection, for example, a 250-m *BL* and *u* = 2.1 m s^{-1} contributes 10-20% of *C'* from 2-km downwind (**Fig. S1**). *C'* is relative to the background concentration, *C*, which is based on concentrations outside the plume's edges and can include environmental gradients from large-scale transport processes.

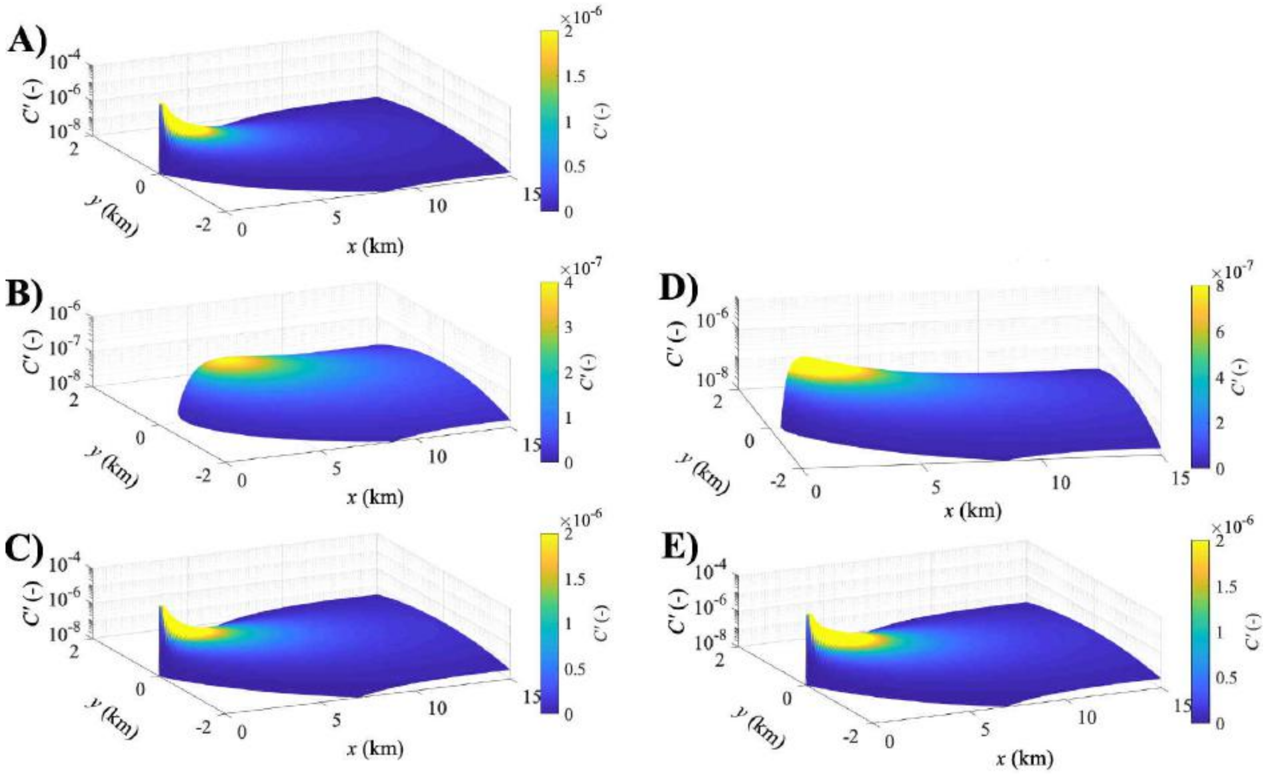

Figure S1: Surface concentration, *C'*, for Gaussian plumes for u=2.1 m s^{-1} **A)** with no planetary boundary layer, *BL*, **B)** reflection from a 250-m *BL* (Eqn. 1, terms 3+4) and **C)** Gaussian plume with 250-m *BL*. **D)** Reflection plume from a 100-m *BL* and **E)** Gaussian plume with 100-m *BL*. Arbitrary *C'* units. Data key on panel.

Parameterization of σ_y and σ_z are:

$$\sigma_y = a(1 + 10^{-4}x)^{-1/2}; \sigma_z = b(1 + cx)^n \,, \qquad \textbf{(S2)}$$

with a, b, and c depending on stability class (Briggs, 1973). Stability class (**Table S2**) is based on solar insolation, I, and u (Hanna et al., 1982). These turbulence parameterizations (**Eqn. S2**) are discrete (**Table S1**), which introduces uncertainty in σ_x and σ_y, particularly at stability class transitions. To remove discretization distortions, a 2nd-order polynomial was fit to the turbulence parameters a, b, and c, for each insolation class with respect to u (**Fig. S2**). The polynomial fit then was evaluated for u to determine a, b, and c for all three insolation classes. Strong, moderate, and weak insolation were fit for class values of I = 800, 500, and 175 W m^{-2}, respectively. The parameterizations are shown in **Fig. S2** and are for $1 < u < 6$ m s^{-1}. Given the coarse nature of the Pasquill classes, no effort was made to optimize; simply, the center u for each class was used in the parameterization.

Table S1. Parameters for atmospheric turbulence parameterizations for different stability classes*

Class		*a*	*b*	*c*	*n*	Class Description
A	*open*	0.22	0.20	0	-	Extremely unstable
B	*open*	0.16	0.12	0	-	Moderately unstable
C	*open*	0.11	0.08	$2x10^{-4}$	-0.5	Slightly unstable
D	*open*	0.08	0.06	0.015	-0.5	Neutral
E	*open*	0.06	0.03	$3x10^{-4}$	-1	Slightly stable
F	*open*	0.04	0.016	$3x10^{-4}$	-1	Moderately stable

*Briggs (1973).

Table S2. Conditions defining Pasquill turbulence classes*

u	I_{Strong}	$I_{Moderate}$	I_{Weak}	Nighttime	Nighttime
m s^{-1}	>700 W m^{-2}	350-700 W m^{-2}	<350 W m^{-2}	**>$^{1}/_{2}$ clouds**	**<$^{3}/_{8}$ cloudiness**
<2	A	A-B	B	E	F
2	A-B	B	C	E	F
4	B	B-C	C	D	E
6	C	C-D	D	D	D
>6	C	D	D	D	D

*from Hanna et al. (1982). *u* is wind speed. *I* is solar insolation.

The Gaussian plume model is for a passive dispersant and assumes that negligible along-wind diffusion, that u, σ_y, and σ_z are vertically and horizontally uniform along its trajectory, that u fluctuations are zero, and that u remains parallel to the x axis (no veering). These assumptions imply an idealized, flat terrain of homogeneous roughness. Violations of these conditions are common in terrestrial settings and can be addressed by model modification, e.g., Briggs (1973); Leifer et al. (2016), the absence of topography and obstacles at sea implies that marine plumes generally satisfy the Gaussian plume requirements.

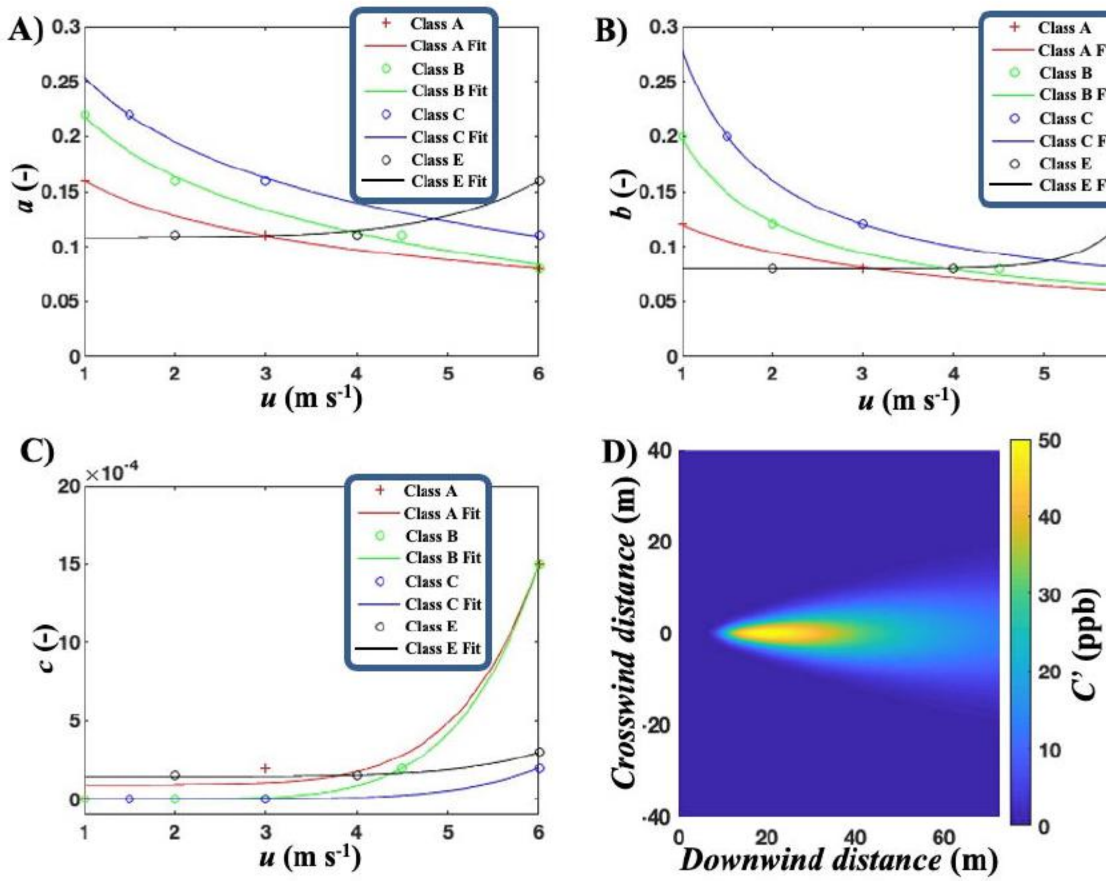

Figure S2: Pasquill turbulence parameters (**Table S1**) and 2nd-order polynomial least-squares linear-regression fits of **A)** *a*, **B)** *b*, and **C)** *c* for solar insolation stability classes (**Table S1**; class data key on figure) versus wind speed, *u*. See text for details. **D)** Gaussian plume surface concentration, C', for 0.47 L min^{-1} emissions, u = 3.5 m s^{-1}, and no boundary layer.

Simulations were conducted for three conditions: infinite planetary boundary layer, i.e., no reflection, a 250-m *BL*, and a 100-m *BL*. The higher, 250-m *BL* only affects *C'* several kilometers downwind, whereas for *BL*=100 m, the reflection affects *C'* far closer to the source and far more strongly. The combined plume and *reflection* flatten the downwind plume near the axis, but with a sharper off-axis decrease in *C'*.

S2 Focused seep areas

Table S3. Location and direction from West Campus Station of informally-named seeps

Seep Area	θ	Latitude, Longitude
La Goleta Seep	152°	34° 23.503'N, 119° 51.193'W
Seep Tent Seep	198°	34° 23.063'N, 119° 53.428'W
Platform Holly	238°	34° 23.392'N, 119° 54.374' W
Trilogy Seep C	178°	34° 23.634'N, 119° 52.702'W
Trilogy Seep B	178°	34° 23.620'N, 119° 52.709'W
Trilogy Seep A	178°	34° 23.603'N, 119° 52.699'W
Patch Seep	140°	34° 21.850'N, 119° 49.755'W
Shane Seep	230°	34° 24.370'N, 119° 53.428'W
IV Super Seep	146°	34° 24.090'N, 119° 52.066'W
Tonya Seep	184°	34° 24.043'N, 119° 52.841'W
Horseshoe Seep	186°	34° 23.799'N, 119° 52.519'W
Rostocker Seep	99°	34° 24.230'N, 119° 50.438'W
Seadog Seep	240°	34° 24.172'N, 119° 54.374'W

*θ – direction from West Campus Station (34.414949°N, 119.879690°W).

S3 Sonar return

The Sept. 2005 seep field survey sonar return, ω, was gridded at spatial resolutions from 11 to 225 m in a coordinate system with origin at West Campus Station, WCS, 34° 24.8969'N, 119° 52.7814'W (**Fig. S3**). See Leifer et al. (2010) for details on the sonar survey data acquisition and analysis. Gridding involves averaging of all ω in each bin followed by a gap-filling low-pass filter. To gap fill, the center bin in a rolling 3x3-bin window which is empty, is replaced by the mean if there are more than 5 non-empty bins in the window. A hybrid 56/22-m gridding scheme gap filled the 22-m grid with the 56-m grid and was used in simulations (**Fig. S3C**).

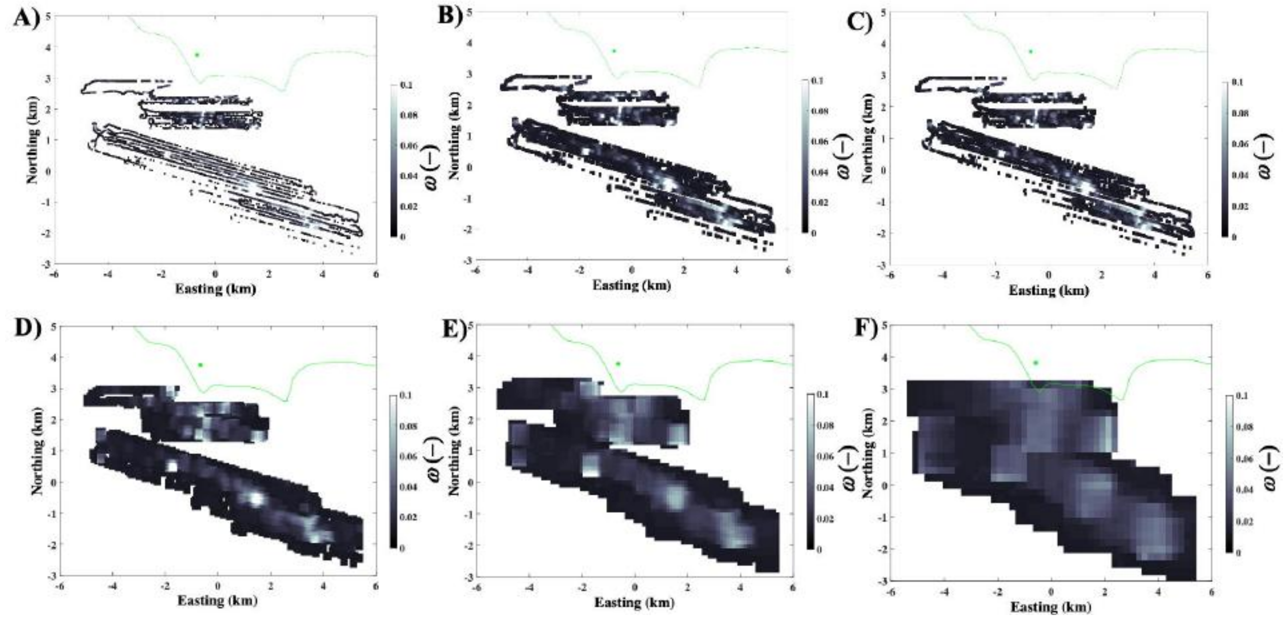

Figure S3: Sonar return, ω, maps for gridding at **A)** 11-m, **B)** 22 m, **C)** 22/56-m **D)**, 56 m, **E)** 110 m, and **F)** 225 m. See text for details. Data key on panels.

The noise level was 0.015 and was identified from a histogram of *ω*, where the *ω* probability distribution shows a power law shift and is the transition from seep distribution to noise domination (**Fig. S4**). Although there clearly is a seep contribution below the noise level, it cannot be segregated from noise and is neglected.

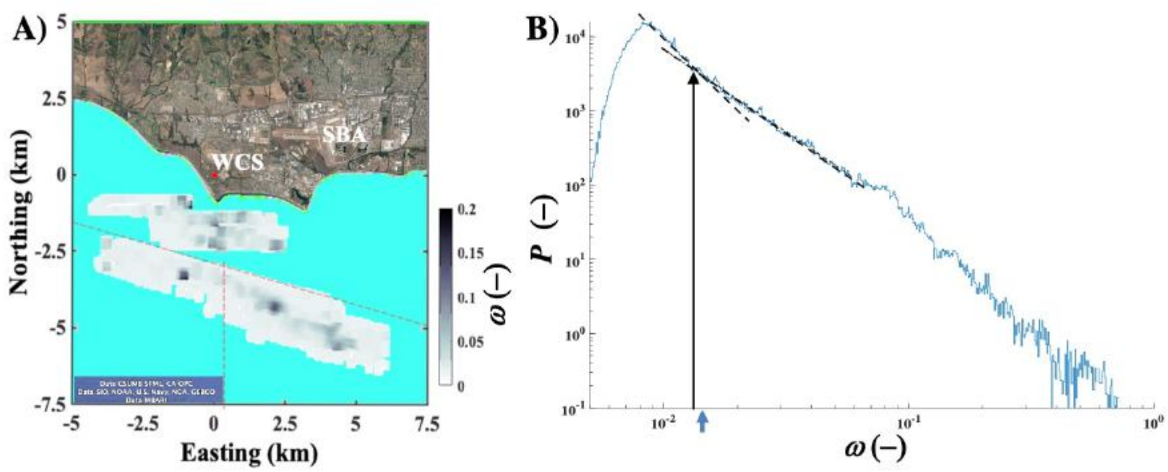

Figure S4: A) 22/56-m gridded 2005 sonar return, *ω*. Green dot shows West Campus Station (WCS) location. Shown in the © Google Earth environment. **B)** Occurrence distribution, *P*(*ω*). Arrow shows noise level based on shift in power law fits to *P* at ω~0.015. Data key on panels. SBA - Santa Barbara Airport.

S4 Gaussian Plume model of an area plume

The model's core routines calculate a Gaussian plume (**Fig. S5A**) for the specified meteorological conditions in a Cartesian coordinate system. Then, the plume is rotated to the wind direction, re-gridded, and normalized to ensure mass conservation (**Fig. S5B**). The rotated plume is translated to each grid cell, scaled to emissions for that grid cell, and finally, all plumes are added (**Fig. S5C**). *C'* at WCS is calculated from the combined seep field emission plume map (**Fig. S5D**).

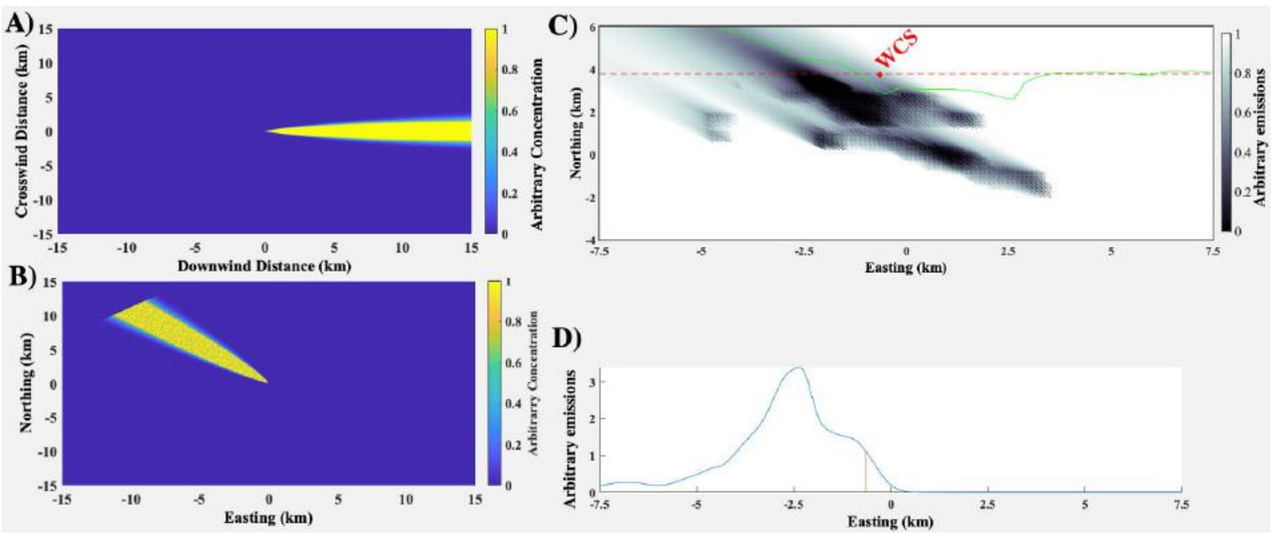

Figure S5: A) Gaussian plume concentration (arbitrary units) for 4 m s^{-1} wind speed and 250 m-thick boundary layer. **B)** Plume rotated to a wind direction, θ, of 135°, regridded, and normalized. **C)** Assembled plumes from all grid cells. Dashed red line shows a constant northing transect through West Campus Station, WCS. **D)** Concentration profile along WCS transect (dashed red line in panel C). Red line shows location of WCS.

S5 Field atmospheric observations

Winds for 28 May 2016 were largely from the east with some modifications near the coast (**Fig. S6**). Winds in Goleta Bay included a strong onshore component, which was absent offshore Isla Vista where the shoreline features tall bluffs (~10-14 m). To the west of COP, winds had a strong offshore component as far as halfway to Naples. Enhancements in the transect offshore west Sands Beach and Haskell Beach are consistent with emissions from shallow waters, beaches, and/or coastal onshore from seepage and/or abandoned oil wells.

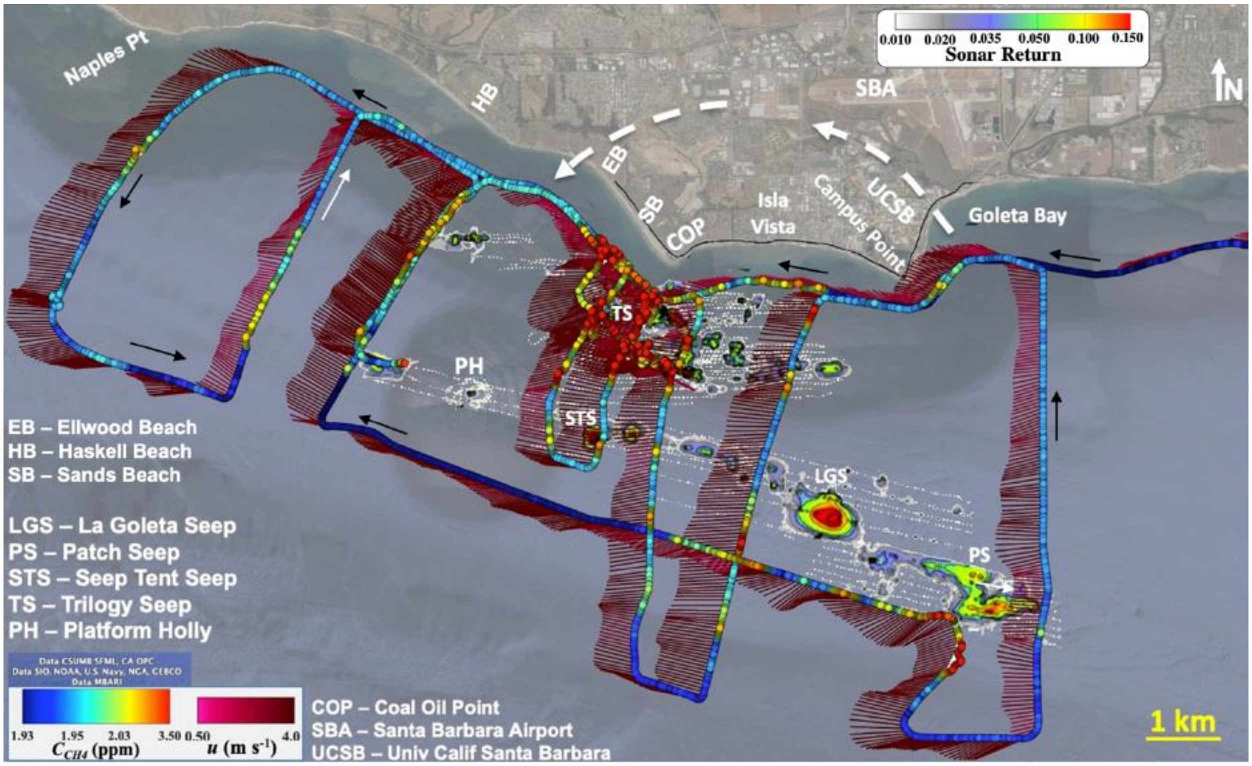

Figure S6: Methane, C_{CH4}, and winds, u, for 28 May 2016. Sonar return map for reference in background. Dashed arrow shows proposed onshore winds; black arrows show travel direction. Shown in Google Earth environment. ©Google Earth. See **Table S3** for locations of informally named seeps.

On 28 May 2016 winds were strongly from the east, which is uncommon, and largely overwhelmed the sea breeze. The easterly winds flow onshore in Goleta Bay and then offshore around Ellwood and Sands Beach, to the west of COP. This likely relates to a combination of the sea breeze in Goleta Bay and the overall easterly flow which in turn drives an offshore flow (by continuity) around Ellwood and Haskell Beaches. This wind flow creates strong convergence and divergence air flows.

S6 West Campus Station data

S6.1 Trends

WCS data show a significant change in 2008 when the station was upgraded from 1-hour to 1-minute time resolution, allowing far higher values of total hydrocarbon concentration, THC, and u (**Fig. S7**). Hereafter, all concentrations and emissions are THC unless otherwise noted. To assess whether the station upgrade introduced biases, $\phi(u)$ prior and post 2008 were compared (**Fig. S7C,**

7D). The slopes of $\phi(u)$ with respect to u for 2 to 4 m s^{-1} are nearly identical for ϕ for the pre- and post-2008 data, the main change is for highest and weakest u, i.e., the range was extended. Moreover, several shifts between subsequent years for u and C have been documented (1997 and 2012 for u, 1997 and 2013 for C), i.e., such shifts in annualized values are not unique to 2008 (**Fig. S8**). This strongly argues that the changes in average, median, and baseline values post 2008 were from better measurement of gusts and weak winds and short positive C anomalies.

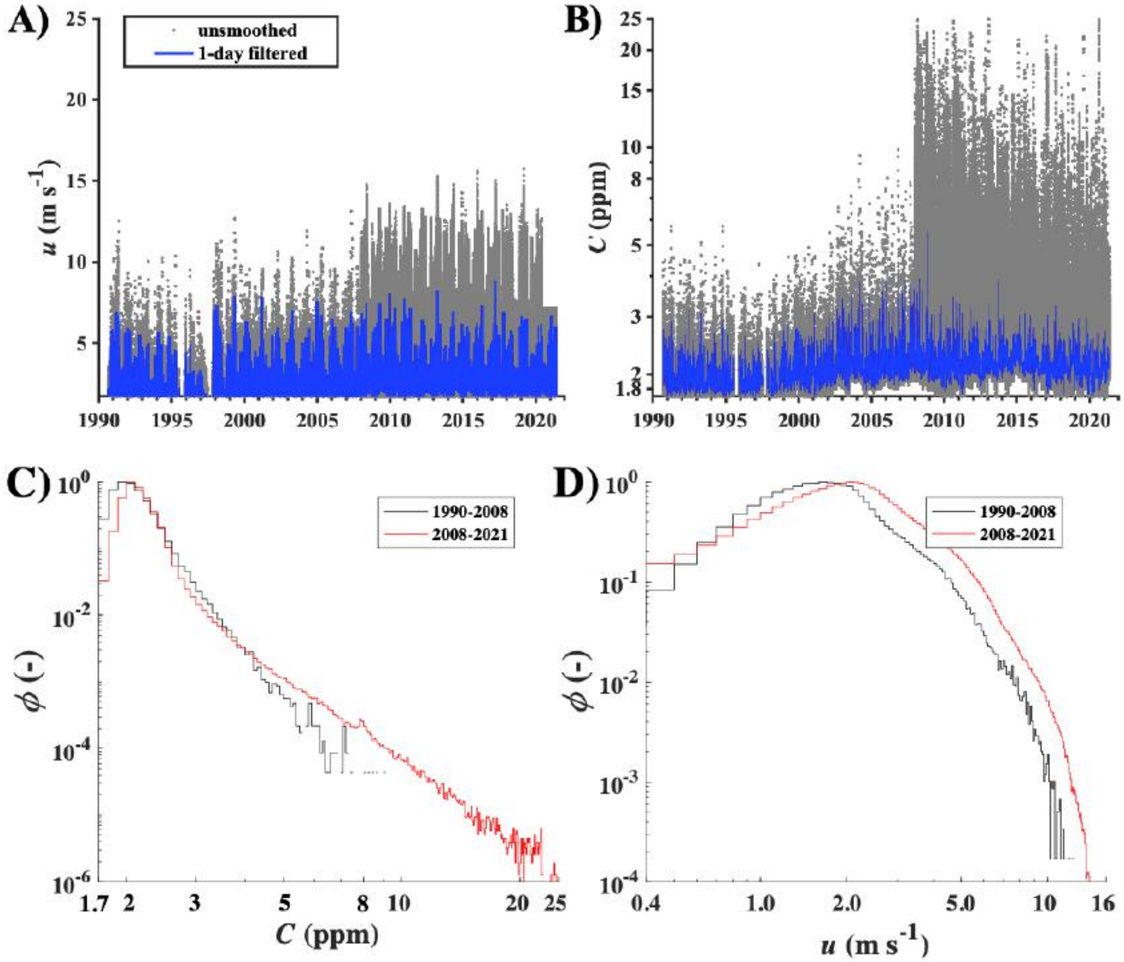

Figure S7: WCS unfiltered and 24-hour smoothed data for **A)** wind speed, u, and **B)** concentration, C. WCS concentration probability distribution, ϕ, for before and after the 2008 upgrade for **C)** u and **D)** C. Data key on panel.

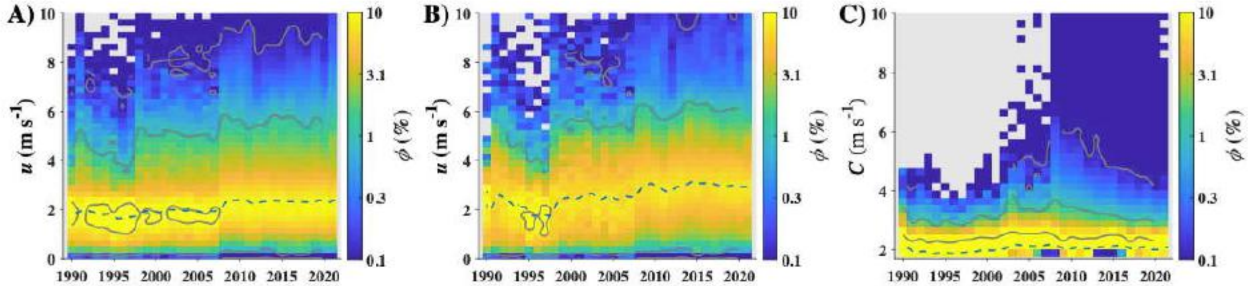

Figure S8: Annual wind speed, u, probability, ϕ, for **A)** all wind directions, θ, **B)** seep directions (135°<θ<270°). Contours at ϕ=0.1, 1, 10%, calculated from 4-year smoothed data. **C)** ϕ for C for seep directions. Annual median (dashed line) shown on all panels. Data key for ϕ on figure.

A linear regression analysis of the wind data showed increasing median u of 0.023 m s^{-1} yr^{-1} and 0.04 m s^{-1} yr^{-1} for all directions and for seep directions, respectively (**Fig. S9A**). This corresponds to an increasing sea breeze (from the seep direction). Summer winds have increased faster than winter winds, 0.043 versus 0.027 m s^{-1}, respectively.

The residual, R, to the Gaussian fit to $C'(\theta)$ showed an overall increasing linear spatial trend of 0.17 ppb degree^{-1} from 175° to 210° (**Fig. S9B**). There is a peak at R~230° that corresponds to Shane Seep and a peak at R~170°, which does not correspond to any named seeps (**Table S3**), but is in the general direction of the inshore seep trend to the east of the Trilogy Seeps (**Fig. 1**).

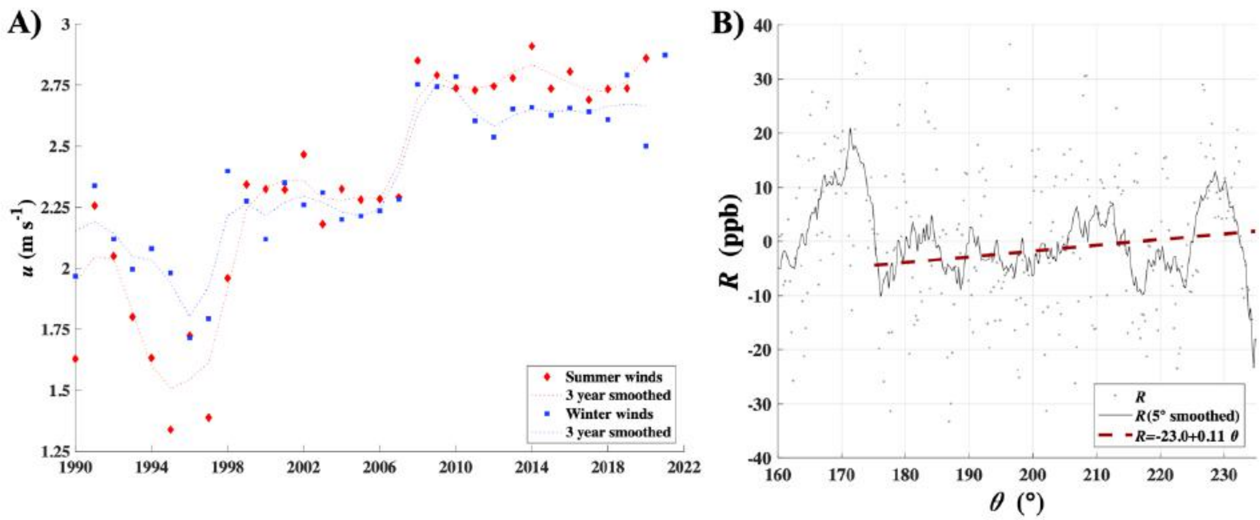

Figure S9: A) Seasonally-segregated, annually-averaged wind speed, u for WCS. Summer is for Julian day 135-250, winter is Julian day 260-130, and three-year rolling-average. **B)** Residual, R, to dual Gaussian plume fit (**Fig. 4A**) to wind-direction resolved concentration, $C(\theta)$, for 1990-2019 for unsmoothed, 5° smoothed, and least-squares, linear-regression analysis fit. Data key on panel.

S6.2 Diurnal

Hourly-segregated averaged u and C for 1991-2007 (**Fig. S10**) show similar overall patterns to 2008-2021 for the seep directions (**Fig. 6**). The station improvements shifted averages, making averaging the entire datasets inappropriate. One difference was the late-afternoon peak in C towards the east-northeast, which was absent in the earlier period. The significant expansion of housing and commercial developments in this direction in recent decades likely underlies this change.

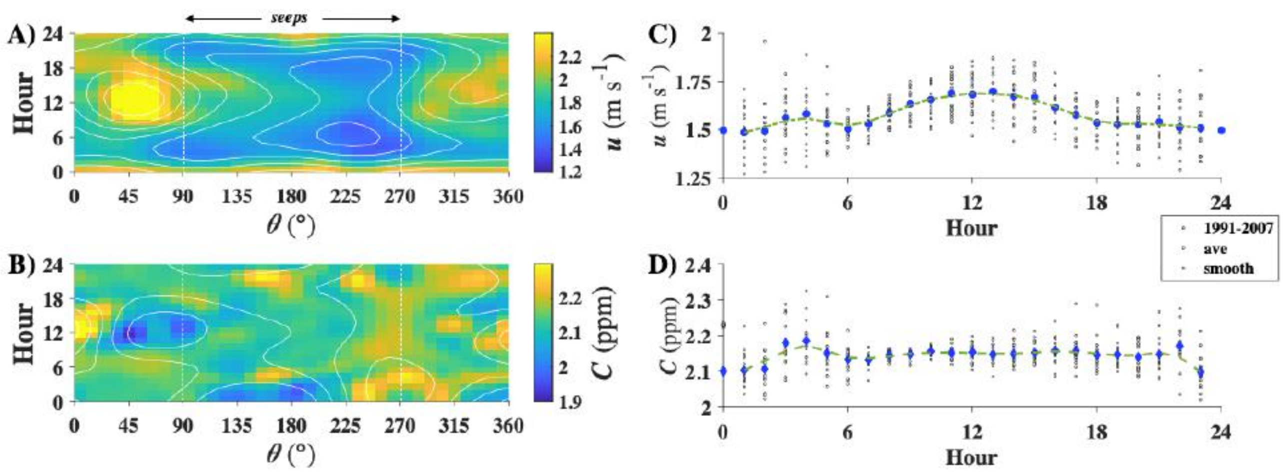

Figure S10: 1991-2007 averaged wind direction, θ, and hourly-resolved **A)** wind speed, u, and **B)** concentration, C. **C)** Seep-direction (90–270°), hourly-averaged wind speed, u_{seep}, and **D)** concentration, C_{seep}, averaged, individual years, and 3-year smoothed. Data key on figure. Midnight data missing due to daily calibration.

S7 Seep field emissions

S7.1 Effect of model wind direction resolution

Emissions simulations are run iteratively, initialized by the sonar distribution, which was multiplied by a scaling factor, $K(\theta)$, initialized with K=22,620, that was applied to $E(x,y)$. Notably, the θ-resolved C'_{Sim} and C'_{Obs} disagree significantly. This is unsurprising as the relationship between ω and seabed emissions is complex (Leifer et al., 2017) with additional complexity arising from transport across the water column. For sensitivity studies, the scaling factor, $K(\theta)$, see **Eqn. 3**, was applied to $E(\theta)$ after each iteration until convergence (<1%), typically within 5 iterations (**Fig. S11**).

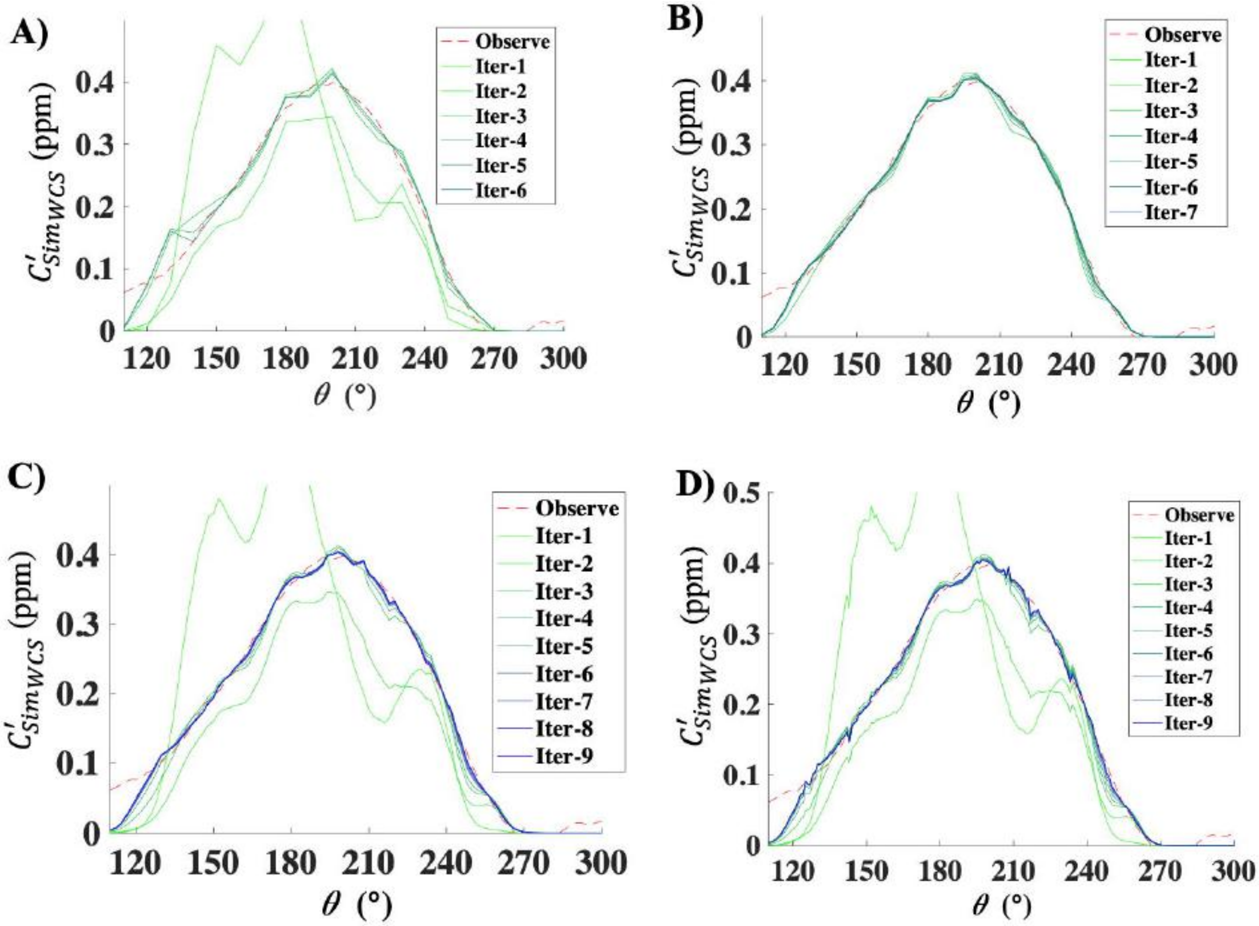

Figure S11: Observed and simulated WCS concentration anomaly, C'_{Obs} and C'_{Sim}, respectively, versus wind direction, θ, for all iterations for 22/56-m sonar map and angular, θ, resolutions, of **A)** 10°, **B)** 5°, **C)** 2°, and **D)** 1°. Data key on figure.

Simulations were conducted with no distance correction, i.e., $K(r,\theta)$ =1 for north offsets of WCS location, Y, from 0 to 3 km. For reference, the inner and outer seep trends are 1.5 and 3.5 km from WCS at their closest direction. Simulations showed a near linear response in E_A to Y (**Fig. S12**), which was applied to as a distance scaling function, $K(r,\theta)$, in all further simulations.

S7.2 Effect of distance to seep field on emissions

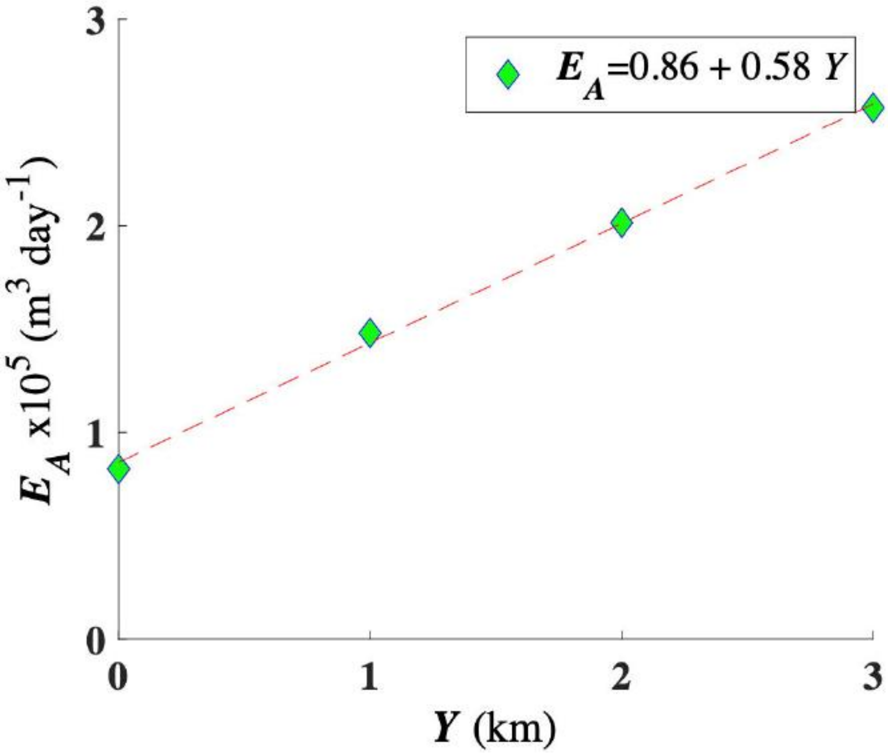

Figure S12: Simulated atmospheric emissions, E_A, with respect to north offset, Y, modeled with no distance varying correction factor, and linear fit shown on panel.

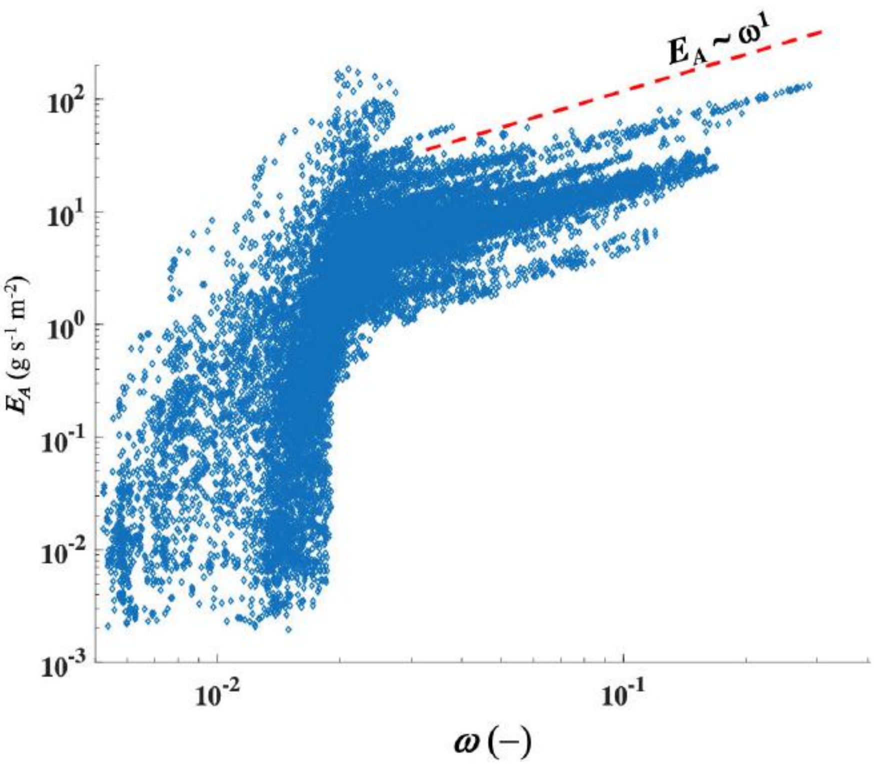

Figure S13: Sonar return, ω, versus derived atmospheric emissions, E_A. Line illustrates unity power law.

S7.3 Sonar return versus atmospheric emissions

Plotting all E_A versus ω shows a non-linear relationship (**Fig. S13**) with E_A increasing very steeply with ω before rolling over for values of E_A in the range 1-10 g s^{-1} m^{-2}. After rolling over, there were several populations of ω-values that increased as a power law with an exponent slightly less than unity. Emissions are the fraction of the seabed emissions that are transferred into the atmosphere, including from adjacent pixels where emissions are from evasion – the simulation was initialized with non-zero ω in neighboring cells to allow the simulation to infer sear-air gas evasion emissions from these cells. This accounts for values of ω less than 0.02 in **Fig. S13**. The highest ω corresponds to the strongest plumes where sonar tends to saturate (Leifer et al., 2017) but dissolved gas evasion emissions to the atmosphere are more efficient due to the upwelling flow, which is more efficient in strong plumes.

S7.4 Emissions Uncertainty

S7.4.1 Angular resolution

Sensitivity to angular resolution, $\delta\theta$, is very weak, <1% for reducing $\Delta\theta$ from 10° to 1°. For example, a resolution of $\delta\theta$=1° produced artifacts and only changed E by 0.3% for reducing $\delta\theta$ from 2° to 1°. $\delta\theta$ resolution affects simulation resolution with coarse resolution blurring the fine-scale sonar structure that is apparent in the 1° simulations (**Fig. S11D**); however, 1° simulations produced overly-quantized results for the hybrid 22/56-m sonar maps including banding artifacts. Thus, θ resolution was 2° outside of several sensitivity simulations.

S7.4.2 Veering

Veering, ψ, was implemented by adding ψ to θ in the calculation of $K(r,\theta)$, i.e., $K(r,\theta+\psi)$. Wind veering emphasized emissions at the field's edges, clearly affecting the seep emissions map. ψ=+10° produced better agreement with the sonar map. Wind veering simulations (**Fig. S14**) overly emphasized emissions at the seep field's edge towards which there was veering, although the no-wind veering simulation also emphasized the western field's seepage. Overall, the ψ =+10° was an improvement. Specifically, it improved the importance of La Goleta Seep compared to the no wind veering simulation and also lessened the enhancement of the western seep field's edge (**Fig. 7B**).

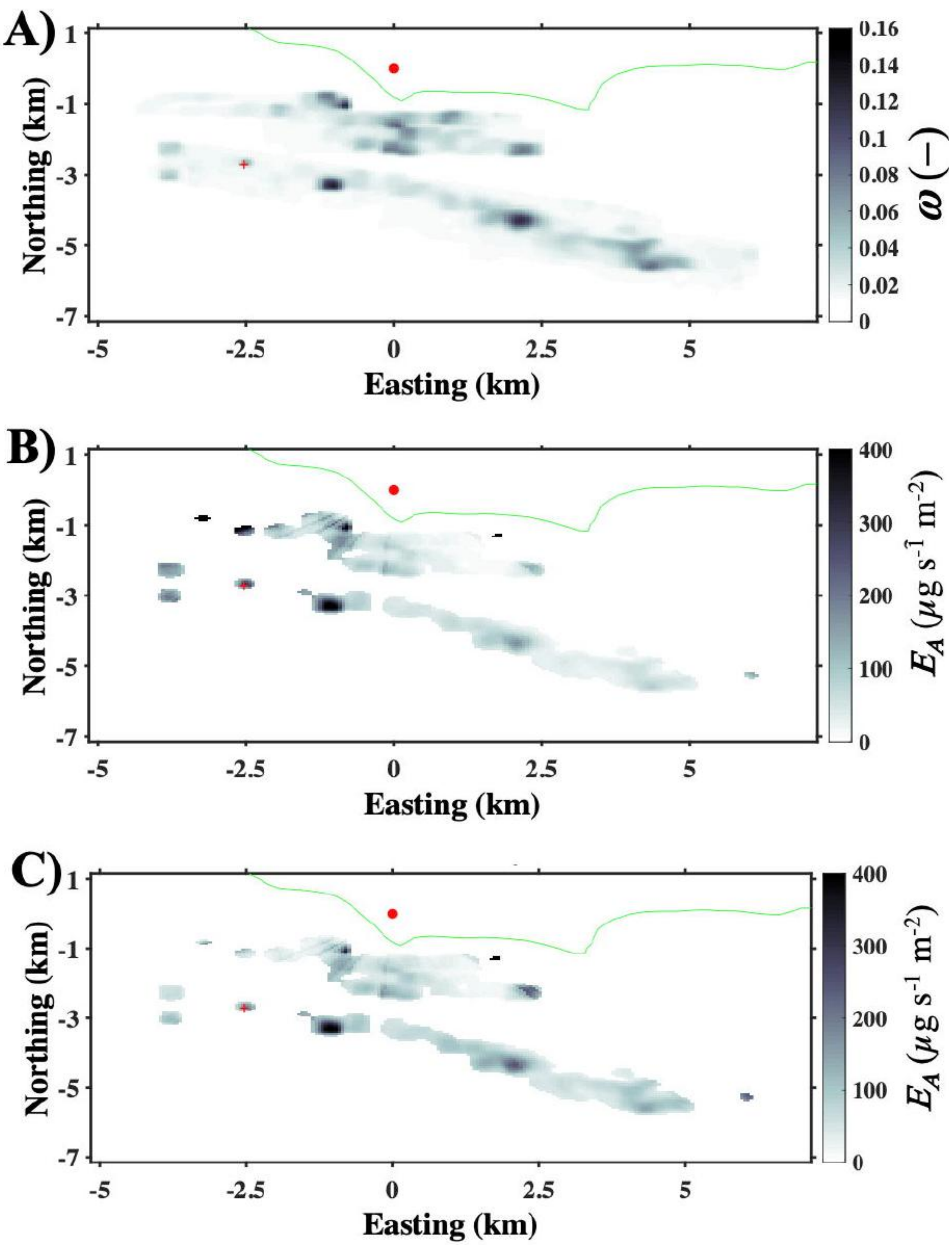

Figure S14: **A)** Sonar return, ω, map gridded to 56-m resolution. **B)** Atmospheric emissions, E_A, map for wind veering, ψ, of **B)** ψ=-10° and **C)** ψ=10°. Data key on figure.

E_A was extremely weakly sensitive to ψ, with ±10° veering corresponding to only a few percent in E_A. This low sensitivity arises because ψ simply shifts emissions to neighboring cells, only changing E_A when neighboring cells have no seepage forcing the model to increase emissions from more distant cells.

S7.4.3 Wind speed

There is a strong sensitivity of E_A to u, particularly for small negative variations, although sensitivity saturated at ±10% with greater sensitivity for lower u. This sensitivity was shown by a series of non-iterative simulations of $C'(\theta)$ for a range of u, showing variations were most strong for very weak wind speeds. Observed u span the range of weak for the east and south to moderate for prevailing (**Fig. S15A**). Instrumentation uncertainty in u is a few percent, thus uncertainty in u arises if WCS winds are unrepresentative due to acceleration or deceleration between the seep field and WCS. C' is highest for $u = 1$ m s^{-1}, which is weaker than actual winds, whereas C' for $u = 8$ m s^{-1} is about a tenth C' for $u = 1$ m s^{-1}. At lower u, there is more "blurring" of plumes from different sources showing less defined structure than higher u. However, u and BL are not independent – by continuity, an increase in u – i.e., acceleration, requires a decrease in BL. Thus, BL sensitivity largely counters u sensitivity, discussed in **Sec. S8.5**.

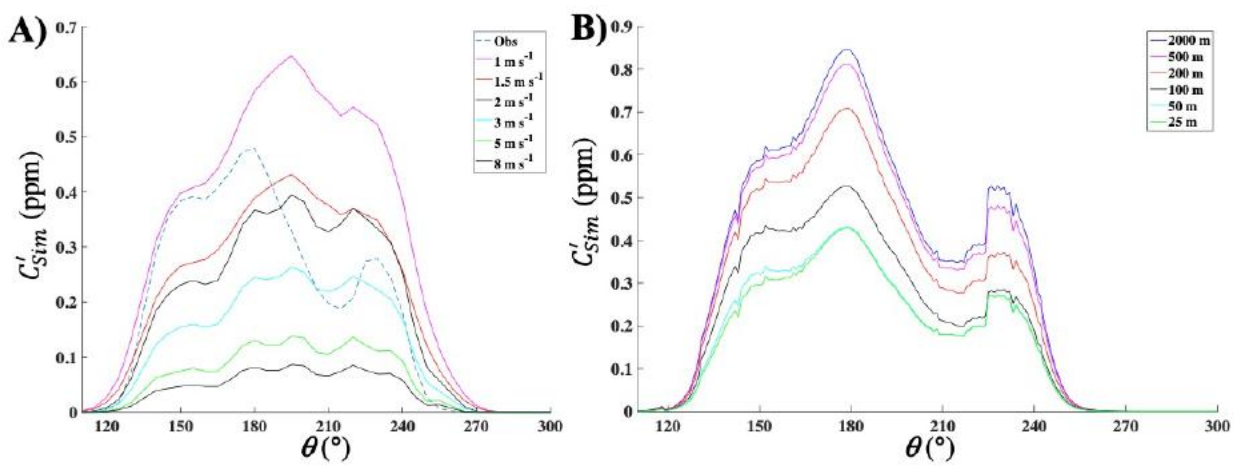

Figure S15: Simulated concentration anomaly, C'_{Sim}, versus wind direction, θ, for WCS for different **A)** wind speed, u, including for the observed $u(\theta)$. **B)** Boundary layer height. $\delta\theta$ resolution is 1°. Data key on figure.

S7.4.4 Boundary layer

BL sensitivity is weakly non-linear and not strong - a 40% reduction in *BL* (250 to 150 m) only decreased E_A by 17%, less so for a 100 m increase to 350 m in *BL* (**Fig. S15B**). The effect of large *BL* changes saturates – for very high *BL*, it has no effect, and for very shallow *BL*, multiple reflections homogenize the boundary layer leaving only dilution driving *BL* sensitivity. Thus, a factor of 40 variation in *BL* corresponds to a 200% change in $C'(\theta)$. Although the nocturnal *BL* is significantly shallower, nocturnal winds largely are the (northerly) land breeze and thus uncommon for the seep direction. *BL* vales for the seep field and WCS are uncharacterized, thus, a 2nd-order polynomial was fit to *BL* versus E_A and averaged (absolute) over possible ranges. For $200<BL<300$ m, the mean absolute value was 3%, 6% for $150<BL<350$ m.

S7.4.5 Concentration

E_A sensitivity to C' is weaker than that of u, particularly for small variations and is linear (**Fig. 9**). C uncertainty arises from drift in the flame ion detector between nightly calibrations. Thus, the difference in concentration before and after calibration is the daily drift as well as any changes in ambient, which should on average be zero, particularly for around midnight when the atmospheric is stable. A 500-point histogram of the total daily drift was calculated and values <±0.2 ppb were fit with a Gaussian function (larger deviations exhibited a broader distribution which, likely resulted from ambient trends) and found a half-width of 170 ppb, or ±85ppb. Thus, the average drift is ~40 ppb dy^{-1}, reducing for annualized values to ~2 ppb dy^{-1} ($1/\sqrt{365}$), i.e., <1% of the C' value of 300 ppb. As such, uncertainty in C' is not a significant contributor to uncertainty in E_A.

S7.4.6 Combined wind and boundary Layer

E_A sensitivity to *BL* largely counters E_A sensitivity to u (**Fig. 9D)**, even when mismatched – a ±40% decrease in *BL* and ±20% increase in u corresponds to a 6% and 9% decrease in E_A, i.e., less than half the mismatch. By continuity, this should be quite small, reflecting lesser changes in pressure, temperature, and topographic forcing. Underlying this weak sensitivity is that the linear sensitivity of E_A to u largely arises from dilution as for *BL*. Note, this weak sensitivity is for a change in *BL* from the offshore to onshore and the resultant change on winds, not a change in the overall (regional) *BL*.

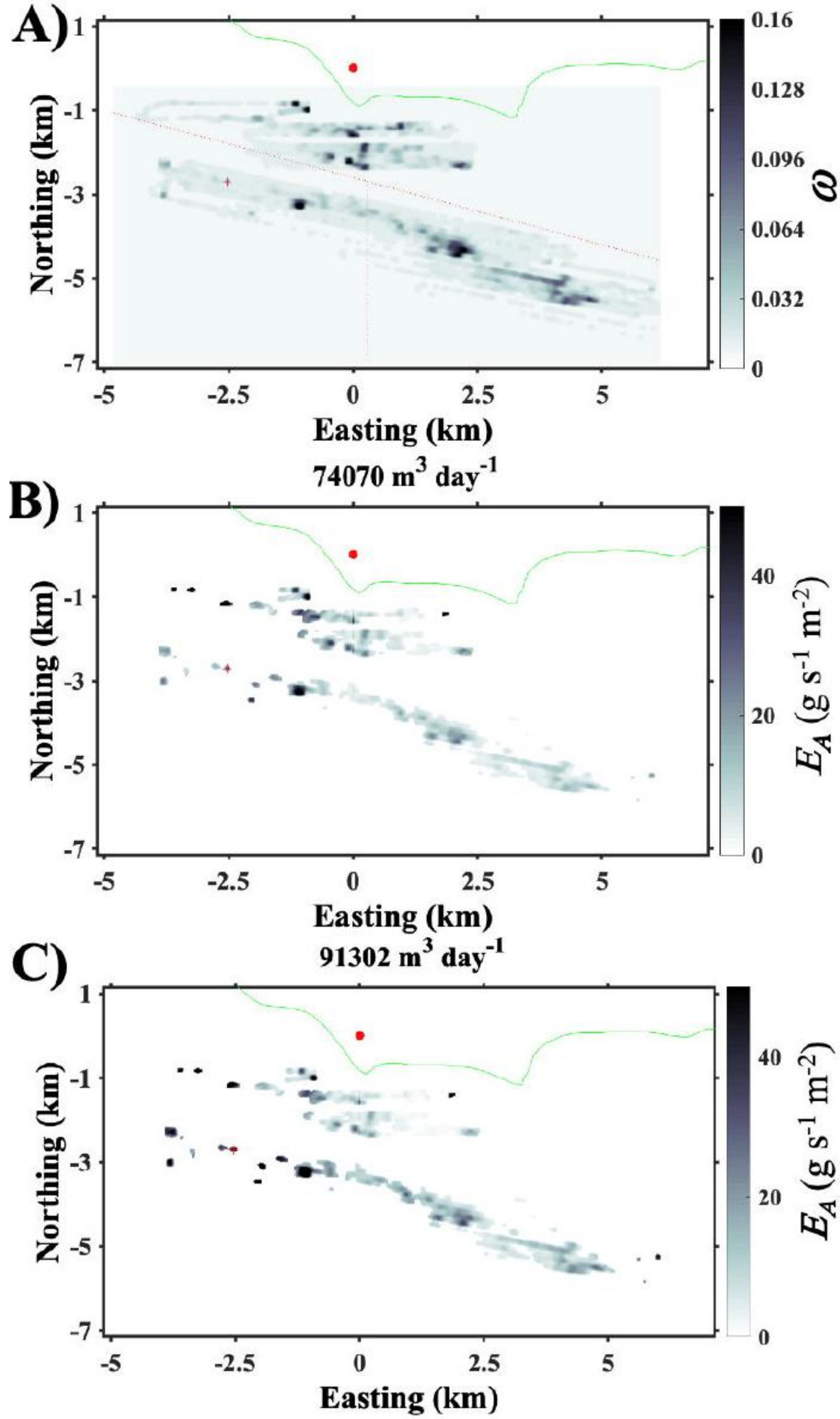

Figure S16: A) Sonar return, ω, map gridded to 56/22-m resolution. Atmospheric emissions, E_A, for inshore/offshore trends relative enhancement, ζ, for **B)** ζ=-25% and **C)** ζ=+25% offshore enhancement.

S7.4.7 Inshore / offshore partitioning

The model cannot determine how to apportion emissions between the inshore and offshore seeps. Simulations found a complex relationship between E_A and ζ (**Fig. 9**) because simulations re-assign some emissions between the seep trends depending on the presence or absence of seepage for θ where there is no seepage on one of the two trends (**Fig. S16**). As such, a potentially strong sensitivity arises from the offshore and onshore seepage trend partitioning with respect to θ. Initial simulations that used a uniform distance partitioning, unrealistically increased inshore seepage compared to ω. Given the similarity in the ω probability distribution between the inshore and offshore trends (**Fig. 8**), i.e., whatever the functional relationship between E_A and ω is, similar ω implies similar E_A.

Sensitivity simulations were run for various shifts in the relative emissions from the inshore and offshore trends – i.e., for +10% inshore -10% offshore, while maintaining a linear variation in $K(r,\theta)$. Sensitivity is strong, and complex – interestingly, reversing between -10° and 10°. This behavior is due to shifting emissions onto different seep areas in the inshore or offshore seep area. As such, for -30%< ζ <+25%, uncertainty ranges from -10% to +5%. Although higher changes in ζ are certainly feasible, both trends source from the same formation, which means on a 30-year time scale (or much shorter), changes in one seep trend likely reflect trends in all seep areas.

Additionally, seepage could shift within the trends – nearer or further - which was assessed by the simulations of north shifts of WCS (**Fig. S12**). Total trend widths are ~300 m for the offshore and 600 m for the inshore, or an average distance deviation of ±75 and 150 m, corresponding to E_A variations of a few percent.

S8 Future data needs and model improvements

S8.1 Key data needs

The driver of uncertainty was whether emissions arose from the inshore or offshore seep trends, which could not be determined from WCS data. A second air quality station located towards the seep field east side would allow triangulation. If the station included a ceilometer, it also could address BL uncertainty in E_A. Long-term BL data would characterize the relationship to solar insolation, diurnal cycle, and winds, allowing application to historical data.

Additionally, THC is a less than ideal seep emission indicator as it can arise from other sources, such as motor vehicles or fires – the station should include speciation, ideally a combination of CEAS analyzers and a gas chromatograph.

The diurnal cycle is poorly constrained by WCS data given that the typical diurnal cycle of strengthening winds in the afternoon also shifts towards the west, with seep field emissions bypassing WCS. Given that an atmospheric plume survey can derive emissions in a couple of minutes, multiple seep areas should be repeat surveyed from morning through early evening to characterize the relationship between wind speed and emissions.

The study focus was marine seepage and neglected terrestrial seepage; however, the data analysis demonstrated that there are notable terrestrial emissions. Further WCS data analysis should assess emissions from Ellwood Field, with onshore surveys searching for seep emissions in neighborhoods by measuring seep gases in the near downwind of abandoned wells and faults, particularly those that intersect with the Ellwood Field.

Finally, the downcurrent dissolved plume's fate is poorly understood as there is an absence of field data collected under typical afternoon winds. A combination of field data collected downwind of the downcurrent plume, ideally in conjunction with water sampling, and further modeling of WCS data can help constrain this emission source and better characterize the fate of COP seep field emissions.

S8.2 Model improvements

The area plume inversion model was used to derive emissions on the field scale and sector scale. Efforts to derive emissions at finer spatial scales were stymied by uncertainty in implementation of wind veering. At the field scale, there was very low sensitivity of E to wind veering (**Fig. S14**); however, simulations without wind veering shifted emissions off of important seeps like Trilogy Seep to nearby seeps that are much smaller than Trilogy Seeps. Additionally, the model assigned emissions to the field edges. Simulations suggested that wind veering that varies with wind direction is needed – consistent with the field observations, i.e., wind veering for the southeast and southwest are different. This is not surprising given the different orientations of the coast on the east and west sides of COP, as well as the topography between WCS and the coast - bluffs (~20 m) on the east side, and their lack to the west (Sands Beach). Additionally, further offshore, wind veering likely becomes less varying across the field and also shifts more towards prevailing. Further field observations are needed to correctly characterize and incorporate wind veering to allow simulations to characterize changes to different areas of the field.

The model's enhancement of seepage at the seep field edges likely is from a combination of wind veering and outgassing emissions from downcurrent plumes. Currently, outgassing in the seep field area is assigned to the nearest seep area along the wind direction. This causes a problem for wind directions in the seep field with no seepage in that direction, including beyond the seep field edges.

Attempts to uniformly assign emissions with distance – i.e., no preferences – led to an unrealistic shift of emissions to the inshore seeps (based on a relative sonar return). A series of simulations where WCS was "shifted" north showed a linear dependency on emissions, and thus the model assigned emissions in any direction linearly with distance. One approach would be to prioritize major seepage over minor seepage in the other seep trend. Such an approach should follow a series of field emissions validation surveys.

There are a number of other model improvements that were not implemented due to computational limits – current simulations take multiple days on a fast workstation (16-core PowerMac, 96 GB RAM, 3.4 GHz). For example, rather than simulating the mean value of winds in a direction, the probability distribution of u in each wind direction, e.g., **Fig. 5A**, could be used, calculating essentially a weighted concentration for comparison with the observed concentration at WCS. This would significantly increase computational load. An additional improvement would be to include a boundary layer height that varied with wind speed and the diurnal cycle, and turbulence parameterizations that are based on solar insolation. Values of boundary layer height and solar insolation could be retrieved from NOAA weather models. It should be noted that the current model complexity required several days to simulate at the highest spatial resolutions on a fast workstation. Finally, higher angular resolution and sonar map resolution (doing one without the other causes non-physical striation) improves the ability to capture changes at different seep areas, but the increased angular resolution introduces more gaps in the seep emissions source function. This could be addressed by adding a "dispersed" source of sea air gas evasion that follows currents.

Supplemental References

Briggs, G. A.: Diffusion estimation for small emissions, NOAA, Air Resources Atmospheric Turbulence and Diffusion Laboratory, Oak Ridge, Tennessee, 87-147, 1973.

Hanna, S. R., Briggs, G. A., and Hosker Jr., R. P.: Handbook on Atmospheric Diffusion, edited by: Smith, J. S., Technical Information Center, U.S. Department of Energy, 110 pp., 1982.

Leifer, I., Kamerling, M., Luyendyk, B. P., and Wilson, D.: Geologic control of natural marine hydrocarbon seep emissions, Coal Oil Point seep field, California, Geo-Marine Letters, 30, 331-338, https://doi.org/10.1007/s00367-010-0188-9, 2010.

Leifer, I., Melton, C., Frash, J., Fischer, M. L., Cui, X., Murray, J. J., and Green, D. S.: Fusion of mobile in situ and satellite remote sensing observations of chemical release emissions to improve disaster response, Frontiers in Science, 4, 1-14, https://doi.org/10.3389/fenvs.2016.00059, 2016.

Leifer, I., Chernykh, D., Shakhova, N., and Semiletov, I.: Sonar gas flux estimation by bubble insonification: Application to methane bubble flux from seep areas in the outer Laptev Sea, The Cryosphere, 11, 1333-1350, https://doi.org/10.5194/tc-11-1333-2017, 2017.